Synthetic Air Data System for Pitot Tube Failure Detection on the Variable Skew Quad Plane

Larocque, F.; De Ponti, T.M.L.; Remes, B.D.W.; Smeur, E.J.J.

DOI
10.2514/6.2025-2609

Publication date
2025

Document Version
Final published version

Published in
Proceedings of the AIAA SCITECH 2025 Forum

Citation (APA)
Larocque, F., De Ponti, T. M. L., Remes, B. D. W., & Smeur, E. J. J. (2025). Synthetic Air Data System for Pitot Tube Failure Detection on the Variable Skew Quad Plane. In *Proceedings of the AIAA SCITECH 2025 Forum* Article AIAA 2025-2609 https://doi.org/10.2514/6.2025-2609

AIAA SciTech Forum
6-10 January 2025, Orlando, FL
AIAA SCITECH 2025 Forum

10.2514/6.2025-2609

Synthetic Air Data System for Pitot Tube Failure Detection on the Variable Skew Quad Plane

Frédéric D. Larocque* and Tomaso De Ponti† and Bart D.W. Remes‡ and Ewoud J.J. Smeur§
Delft University of Technology, 2629 HS Delft, The Netherlands

Pitot tube-free airspeed estimation methods exist for fixed-wing and multirotor configurations, but lack direct applicability to hybrid unmanned air vehicles due to their wide flight envelope and changing dynamics during transition. This work proposes a novel synthetic air data system for the Variable Skew Quad Plane (VSQP) hybrid vehicle to allow airspeed estimation from hover to high speed forward flight and provide pitot tube fault detection. An Extended Kalman Filter fuses Global Navigation Satellite System (GNSS) and inertial measurements using model-independent kinematics equations to estimate wind and airspeed without the use of the pitot tube. The filter is augmented by a simplified vehicle force model. Pitot tube fault detection is achieved with a simple thresholding operation on the pitot tube measurement and the airspeed estimation residual. Accurate airspeed estimation was validated with logged test flight data, achieving an overall 1.62 m/s root mean square error. Using the airspeed estimation, quick detection (0.16 s) of a real-life abrupt pitot tube fault was demonstrated. This new airspeed estimation method provides an innovative approach for increasing the fault tolerance of the VSQP and similar quad-plane vehicles.

Nomenclature

Abbreviation	Description	Unit
AR	Aspect Ratio	-
a_x, a_y, a_z	Acceleration in Body Frame	$\mathrm{m\,s^{-2}}$
C_L	Lift Coefficient	-
C_d	Drag Coefficient	-
d	Diameter of Propeller	m
e	Oswald Factor	-
F	Force	N
$f(x,u)$	State Dynamics	-
$g(x,u)$	Output or Measurement Dynamics	-
$\boldsymbol{G}$	Control Effectiveness	-
g	Gravity	$\mathrm{m\,s^{-2}}$
K	Gain, Parameter or Coefficient	-
L	Lift	N
m	Mass	kg
p, q, r	Angular Rate in Body Frame	$\mathrm{rad\,s^{-1}}$
$\boldsymbol{P}$	State Error Covariance Matrix	-
$\boldsymbol{Q}$	Process Noise Covariance Matrix	-
$\boldsymbol{R}$	Measurement Noise Covariance Matrix	-
$\boldsymbol{r}$	Residual	-
S	Surface, Area	$\mathrm{m^2}$
T	Thrust	N
$\boldsymbol{u}$	Input vector	-
u, v, w	Velocity in Body Frame	$\mathrm{m\,s^{-1}}$
V_a	Airspeed Norm	$\mathrm{m\,s^{-1}}$

---

[*] M.Sc. Student, Faculty of Aerospace Engineering, MAVLab.
[†] Ph.D. Candidate, Faculty of Aerospace Engineering, MAVLab
[‡] Researcher, Faculty of Aerospace Engineering, MAVLab.
[§] Assistant Professor, Faculty of Aerospace Engineering, MAVLab.

Abbreviation	**Description**	**Unit**
V_p	Propeller axial airspeed	$\mathrm{m\,s^{-1}}$
$\boldsymbol{v}_a$	Airspeed Vector	$\mathrm{m\,s^{-1}}$
$V_x^{NED}, V_y^{NED}, V_z^{NED}$	Ground Velocity in Earth Fixed Frame	$\mathrm{m\,s^{-1}}$
$\boldsymbol{v}_w$	Wind Velocity Vector	$\mathrm{m\,s^{-1}}$
$\mathbf{w}$	Noise	-
$\boldsymbol{x}$	State	-
x_b, y_b, z_b	Body axis	-
$\boldsymbol{y}$	Innovation	-
$\boldsymbol{z}$	Measurement	-
Z	Threshold	-
α	Angle of Attack	rad
β	Sideslip Angle	rad
Λ	Wing Skew Angle	°
μ_x, μ_y, μ_z	Wind Velocity in NED Frame	$\mathrm{m\,s^{-1}}$
ρ	Density	$\mathrm{kg\,m^{-3}}$
σ^2	Variance	-
ϕ, θ, ψ	Euler angles	rad

I. Introduction

Hybrid Unmanned Air Vehicles (UAVs) are versatile vehicles capable of flying in both fixed-wing and Vertical Takeoff and Landing (VTOL) configurations. They leverage efficient wing-derived lift and achieve high cruising speeds, while also enabling seamless transitions to hover flight, providing precise VTOL capabilities. Hybrid UAVs require advanced control systems to stabilize their flight in various flying configurations.

Airspeed is one of the most vital measurements required for stable flight as aerodynamic forces vary with airspeed. Typically, a pitot tube is used to derive airspeed from dynamic pressure measurements. Unlike on larger aircraft, low-cost pitot tubes normally used on UAVs are particularly prone to water blockage due to the absence of a drain tube. The pressure slowly or immediately drops, resulting in a reduced or zero airspeed reading [1]. When flight controller parameters are scheduled with airspeed, any sustained airspeed measurement fault can lead to a loss of stability and ultimately the loss of the vehicle.

For larger vehicles, redundancy and a voting scheme can be used to isolate faulty pitot tubes and maintain a reliable airspeed estimation [2]. On smaller UAVs, such a strategy cannot be easily implemented due to weight and space constraints. Additionally, if one pitot tube is subjected to water blockage when flying in highly humid environment, it is highly likely that other pitot tubes would suffer from the same failure, as their failure modes are not independent [3]. It is therefore highly pertinent to estimate airspeed using other sensors on the vehicle to ultimately identify pitot tube failures.

(a) VSQP at Λ = 0°, in quad-mode configuration, with the propellers' rotation conventions used.

(b) VSQP at Λ = 45°, in transition

(c) VSQP at Λ = 90°, in forward flight configuration, with axes definitions used.

Fig. 1 Different skew angle on the VSQP Prototype. In quad-mode configuration 1a, the wing is placed over the fuselage and hover motors are extended. In forward flight configuration 1c, the wing is completely extended and hover motors are stowed in the fuselage for reduced drag.

Synthetic air data systems or the estimation of airspeed without the use of a pitot tube is a well-explored topic for fixed-wing airliners. Different strategies can be used to fuse measurements from sensors such as Global Navigation

Satellite System (GNSS), Inertial Measurement Unit (IMU), angle of attack and side-slip vanes to obtain an estimation of airspeed and wind [1, 4]. Rhudy et al. [5] use measurements from such sensors and wind triangle kinematics equations (see Fig. 2) to derive airspeed and wind estimations for fixed-wing vehicles. As a model-independent estimation method, it can be applied to different vehicles with minimal additional work, but requires angle of attack and side-slip measurements.

When such measurements are not available, a model of the fixed wing vehicle can be used to derive airspeed. Youn et al. [6] explored the use of the z-axis accelerometer and knowledge of the wing's and elevator's C_L curve to estimate airspeed. For hybrid vehicles such as the Variable Skew Quad Plane (VSQP), which transitions from hover flight to forward flight, relying solely on such a strategy is not feasible. Airspeed needs to be known during the transition, before lift starts being generated by the wing. Hansen and Blanke [7] used a similar approach on the drag axis, linking propeller rotational speed to an airspeed estimation, with the vehicle's drag coefficient being known.

Because of its hybrid nature, the VSQP's airspeed estimation also needs to be assessed in the hover flight portion of its mission. A simple strategy for airspeed estimation for multirotors links the vehicle's inclination angle to the airspeed using wind tunnel data assuming a constant drag coefficient [8]. Hattenberger et al. [9] show that rotor drag is the main contributor to drag forces on a multirotor and is linear to airspeed. A constant or varying estimation of rotor drag [10] can be used to estimate airspeed, knowing that the only forces acting on the multicopter come from the rotors' thrust, drag or gravity. However, the assumptions used for these methods do not hold for hybrid vehicles that present additional actuators that can generate forward thrust, a varying drag coefficient and a fuselage that, at higher airspeed, might generate more drag than the rotors themselves.

The direct applicability of fixed-wing and multirotor synthetic air data methods to hybrid vehicles is limited. Therefore, the main goal of this work is to obtain a synthetic air data system capable of accurately estimating airspeed throughout the VSQP's flight envelope using existing sensors such as GNSS and IMU. With an accurate estimation of airspeed, pitot tube faults can be detected and effectively addressed. Although this research focuses on the application of synthetic airspeed estimation for the VSQP platform, it can be applied after some modifications to hybrid vehicles with a similar quad-plane configuration.

This work provides an Extended Kalman Filter (EKF) with model-independent state equations based on kinematics, augmented with a 3 body axes simplified model of the vehicle. The covariance of measurements is scheduled according to the flight phase, taking advantage of the axis providing the most accurate airspeed estimation. A simple pitot tube fault detection is achieved using a residual based thresholding method. The main contributions of this work are: 1) reliable airspeed estimation in the whole flight envelope of a hybrid vehicle, 2) a model of the VSQP with sufficient fidelity to estimate airspeed depending on the flight phase and 3) pitot tube fault detection on actual flight test data with a failure. To the best of the authors' knowledge, this is the first synthetic air data system designed for a hybrid vehicle such as the VSQP.

II. The Variable Skew Quad Plane

The VSQP was designed as a derivative of the well-known quad-plane platform [11]. In hover flight, the VSQP operates as a normal quadrotor, powered by two motors fixed to its fuselage and by two motors arranged perpendicular to the wing, as shown in Fig. 1a. The wing is positioned over the fuselage to minimize susceptibility to wind gusts and reduce the landing footprint. The wing-motor assembly can be rotated 90° around its z axis to transition from hover (defined as $\Lambda = 0°$) to forward flight (defined as $\Lambda = 90°$), as shown in Fig. 1c. Drag is reduced by retracting the hover motors inside the fuselage. In forward flight, thrust is produced by a pusher motor while control is achieved using normal aerodynamic flight controls on the wing and tail. The vehicle is equipped with a pitot tube, GNSS receiver and IMU.

Due to its variable skew wing, the VSQP possesses certain characteristics in common with the oblique flying wing, a manned aircraft concept where the whole wing is skewed around its center axis. Lift, drag, side force generated by the wing all become function of the skew angle [12]. Thus, modelling the vehicle and designing a conventional flight controller based on axis decoupling pose significant challenges.

An Incremental Nonlinear Dynamic Inversion Control (INDI) controller was developed by Van Wijngaarden and Remes [13] and De Ponti et al. [14] for both the stabilization inner loop and guidance outer loop for the VSQP. It requires limited model knowledge, at the expense of increased sensor dependency. The vehicle's nonlinear dynamics can be inverted using the control effectiveness of actuators u on the vehicle's state dynamics $f(x, u)$ to obtain a linear system, easily controllable using classical control methods. The control effectiveness is the jacobian of fx, u with respect to u and can be obtained analytically or using a least square estimation with flight test data [15, 16].

The inner loop's control effectiveness of the aerodynamic control surfaces (ailerons, elevator and rudder) and the outer loop's control effectiveness of the wing are both dependent on airspeed as these actuators are lifting surfaces. Additionally, to perform transition, the wing is skewed according to a schedule that aims to minimize power consumption and maximizes overall control effectiveness [14]. The result is an optimal wing skew angle for the current airspeed. Loss of airspeed data following a pitot tube failure leads to incorrect control effectiveness for the inner and outer loops and an incorrect wing skew position. If sustained, the fault can lead to the vehicle's loss of stability.

III. Model-Independent Airspeed Estimation

GNSS measurements can provide precise ground speed $\boldsymbol{v}_g$ information. Airspeed $\boldsymbol{v}_a$ can be derived using the wind triangle, knowing the wind $\boldsymbol{v}_w$. The wind triangle is visualized in Fig. 2 and is expressed in vector form as:

$$\boldsymbol{v}_g^E = \boldsymbol{v}_a^E + \boldsymbol{v}_w^E. \tag{1}$$

Note that ^{E} represents the earth-fixed reference frame defined by the North, East, Down (NED) axes, and ^{b} indicates the body coordinate frame. The axes used in this work are defined in Fig. 1c. The side slip angle β is defined as the angle between the aircraft airspeed $\boldsymbol{v}_a$ and its plane of symmetry. The rotation matrix $\boldsymbol{R}_{Eb}$ is used to transfer from body to earth fixed frame to obtain:

$$\begin{bmatrix} V_x^E \\ V_y^E \\ V_z^E \end{bmatrix} = \boldsymbol{R}_{Eb} \begin{bmatrix} u \\ v \\ w \end{bmatrix} + \begin{bmatrix} \mu_x \\ \mu_y \\ \mu_z \end{bmatrix}, \tag{2}$$

where $\boldsymbol{\mu}$ is the wind velocity in NED frame.

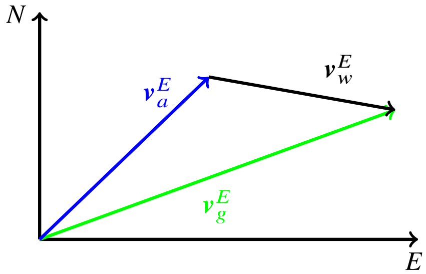

Fig. 2 Wind triangle between airspeed, ground speed and wind speed. Airspeed can be derived from a subtraction between ground speed and wind speed.

In most cases, the wind is not known and must be estimated simultaneously with airspeed. An EKF can be used to estimate the airspeed by assuming slow changing wind magnitude and direction [5].

The state transition dynamics for the velocities in the body frame are expressed as:

$$\begin{bmatrix} \dot{u} \\ \dot{v} \\ \dot{w} \end{bmatrix} = -\left(\begin{bmatrix} p \\ q \\ r \end{bmatrix} + \mathbf{w}^{\omega} \right) \times \begin{bmatrix} u \\ v \\ w \end{bmatrix} + \boldsymbol{R}_{bE} \begin{bmatrix} 0 \\ 0 \\ g \end{bmatrix} + \begin{bmatrix} a_x \\ a_y \\ a_z \end{bmatrix} + \mathbf{w}^a. \tag{3}$$

The kinematics equations themselves present no process noise. Angular rate noise $\mathbf{w}^{\omega}$ and acceleration noise $\mathbf{w}^a$ are added as zero mean Gaussian process noise. Acceleration and angular rates are assumed to be bias free as they are obtained from an independent attitude and position EKF removing bias.

Wind is modeled as a random walk process, as Rhudy et al. [17] showed it to lead to lower airspeed error standard deviation compared to a Gauss-Markov wind model. The wind state dynamics are modeled with zero mean Gaussian process noise $\mathbf{w}^{\mu}$:

$$\dot{\boldsymbol{\mu}} = \mathbf{w}^{\mu} \tag{4}$$

The original implementation of this model-independent airspeed method by Rhudy et al. [5] requires angle of attack and side-slip vane measurements. As the VSQP is not equipped with them, they are replaced by model-dependent airspeed estimation using the vehicle's accelerations. These additional measurements serve a dual purpose, as they also help accelerate wind estimation convergence when the vehicle is not moving relative to the ground or is moving in a straight line. They provide an additional airspeed estimation source. Indeed, to converge on a valid wind estimation using the model-independent method, the vehicle must perform turns, to change the orientation of wind in relation to the vehicle's ground track.

IV. Model-Aided Airspeed Estimation

Specific forces acting on the vehicle can be derived from the different body axes accelerations. The vehicle is modeled by separating it in different components that generate forces: fuselage, hover propellers, wing, ailerons, pusher propeller, elevator and rudder. Ailerons, elevator and rudder are assumed to generate forces that are negligible compared to other components or average to zero on a long horizon. As such, the measured acceleration relates to the sum of forces from the fuselage, hover motors, wing and pusher motor:

$$\boldsymbol{a} = \frac{1}{m}(\boldsymbol{F}_f + \boldsymbol{F}_h + \boldsymbol{F}_w + \boldsymbol{F}_p). \tag{5}$$

A. Fuselage

Drag is modeled as:

$$D = \frac{1}{2}\,\rho\, V_a^2\, S\, C_d. \tag{6}$$

The fuselage is assumed to have a constant drag coefficient and to generate negligible lift. By grouping constant parameters and assuming that the angle of attack is small so that $u \approx V_a$, the force generated by the fuselage is defined as proportional to u squared:

$$F_{x_f} = K_{x_f}\, u^2. \tag{7}$$

The side force is estimated by assuming that part of the fuselage's drag force D_f is projected on the y body axis when side-slip angle β is present [18]:

$$\sin\beta = \frac{-F_{y_f}}{D_f}. \tag{8}$$

Using a small angle approximation on β, substituting Eq. 6 into Eq. 8 and combining constant parameters, the side force generated by the fuselage can be written as:

$$F_{y_f} = K_{y_{f\beta}}\, \beta\, V_a^2. \tag{9}$$

B. Pusher Propeller

Standard definitions for propellers aerodynamic coefficient define a propeller's thrust coefficient C_T:

$$C_T = \frac{T}{\rho\, \omega^2\, d^4}, \tag{10}$$

where ω is the propeller's rotational speed and d its diameter. Test data shows that the thrust coefficient is proportional to the advance ratio $J = \frac{V_p}{\omega\, d}$ [19]:

$$C_T = a\, J + b, \tag{11}$$

where a and b are coefficients experimentally found and V_p the propeller axial flow speed.

Isolating thrust in Eq. 10 and substituting the thrust coefficient from Eq. 11, the thrust can be modeled:

$$T = \rho\, d^3\, a\, \omega\, V_p + b\, \rho\, \omega^2\, d^4. \tag{12}$$

An additional term proportional to airspeed ($K_{x_{p3}}$) is added to better fit wind-tunnel data. It modifies the RPM at which the propeller starts generating thrust depending on airspeed.

For the pusher propeller, the propeller axial flow V_p corresponds to body velocity u. Grouping all constant parameters, thrust generated by a propeller is obtained:

$$T_{x_p} = K_{x_{p1}}\, \omega_p^2 + K_{x_{p2}}\, \omega_p\, u + K_{x_{p3}}\, u. \tag{13}$$

C. Hover Propellers

The hover propellers are modeled in a similar way to the pusher propeller. Flow perpendicular to the propeller's axis of rotation can increase thrust given a constant rotational speed [20]. As the hover motors are to be used mainly in low-speed hover flight, this effect is assumed to be negligible. Axial flow V_p is also assumed to be 0, as the vehicle's climb speed in quad mode is generally low. These assumptions lead to another derivative of Eq. 12, where the average hover propeller rotational speed ω_h is used:

$$T_{z_h} = K_{z_h}\,\omega_h^2. \tag{14}$$

In cross flow, hover propellers mostly generate drag due to a linear difference in local airspeed for the advancing and retreating blade of a rotor. Rotor drag is known to be proportional to the product of rotor RPM and airspeed [21]. Assuming RPM to be constant in hover, hover motors can be modeled as generating drag linear to the incoming airflow [9]:

$$F_{x_h} = K_{x_h}\,u \tag{15}$$

$$F_{y_h} = K_{y_h}\,v. \tag{16}$$

D. Wing

Classical lift and drag forces are defined as perpendicular to the airflow on the wing. At non-zero angles of attack, part of the lift and drag are projected in the x and z body axes:

$$F_x = L\ \sin\alpha - D\ \cos\alpha \tag{17}$$

$$F_z = -L\ \cos\alpha - D\ \sin\alpha. \tag{18}$$

Eq. 17 and 18 can be further expanded by developing the lift and drag equations. Lift is modeled in its usual form

$$L = \frac{1}{2}\rho\, V_a^2\, S\, C_L. \tag{19}$$

The lift coefficient can be assumed to change linearly with the angle of attack

$$C_L = C_{L_\alpha}\,\alpha + C_{L_0}. \tag{20}$$

with C_{L_0} being the lift coefficient value at 0° angle of attack.

Additionally, assuming constant air density ρ and wing surface S, and substituting Eq. 20 into Eq. 19, constant terms can be grouped together to lead to a formulation of lift as a function of the angle of attack multiplied by airspeed squared:

$$L = (K_{L_0} + K_{L_1}\,\alpha)V_a^2. \tag{21}$$

A similar strategy can be used with drag as well. The drag coefficient can be modeled with the simple parabolic drag polar:

$$C_d = C_{d_0} + \frac{C_L^2}{\pi\, AR\, e}. \tag{22}$$

The aspect ratio AR and Oswald efficiency e are assumed to be constant. Substituting Eq. 20 and Eq. 22 into Eq. 6 and grouping all common constants, a second order polynomial multiplied by airspeed squared is obtained:

$$D = (K_{D_0} + K_{D_1}\,\alpha + K_{D_2}\,\alpha^2)\,V^2. \tag{23}$$

Using the small angle approximation on Eq. 17 and 18, substituting in Eq. 23 and 21 and removing third order terms as they are of small magnitude compared to first and second order terms, a formulation of forces in the x and z axis due to lift and drag is obtained:

$$F_x = (K_{x_0} + K_{x_1}\,\alpha + K_{x_2}\,\alpha^2)\,V^2 \tag{24}$$

$$F_z = (K_{z_0} + K_{z_1}\,\alpha + K_{z_2}\,\alpha^2)\,V^2. \tag{25}$$

Lift for the skewed wing is assumed to be derived from the chordwise airspeed V_n component of airspeed V_a [14]:

$$V_n = V_a \sin\Lambda, \tag{26}$$

where Λ is the skew angle.

When fully retracted, the wing can still generate some lift and drag, captured by the addition of a constant term ($K_{x_{w3}}$). It follows that force in the x and z body axes can be modeled as a function of airspeed, skew angle and angle of attack:

$$F_{x_w} = (K_{x_{w_0}} + K_{x_{w_1}}\,\alpha + K_{x_{w_2}}\,\alpha^2)\,(\sin^2\Lambda + K_{x_{w3}})\,V_a^2 \tag{27}$$

$$F_{z_w} = (K_{z_{w_0}} + K_{z_{w_1}}\,\alpha + K_{z_{w_2}}\,\alpha^2)\,(\sin^2\Lambda + K_{z_{w_3}})\,V_a^2. \tag{28}$$

The wing generates a side force when it is skewed as some of its resultant aerodynamic force is projected in the y body axis. As such, it is expected that side force will be a function of skew angle, angle of attack and airspeed. To simplify the model, the side force is modeled at a singular angle of attack that should be representative of the vehicle's angle of attack during transition. As transition occurs rapidly in 4–5 s, this model offset error should have limited impact on the airspeed estimation. Wind tunnel testing lead to an empiric relationship between side force, skew angle and x-body axis airspeed:

$$F_{y_w} = \left(K_{y_w}\;\sin\Lambda\cos^2\Lambda\right)\,V_a^2. \tag{29}$$

A model of side force based on the physical phenomena of lift and drag was attempted but lead to model offset when validated with wind tunnel data. Refer to Appendix A for additional information.

The coefficients for the all the previous models are obtained with wind tunnel experimentation and adjusted slightly with flight test results. Appendix A reviews the wind tunnel data validation campaign completed.

E. Model-Dependent EKF Formulation

With the whole aircraft model developped, the measurement equations for the EKF can be written as the sum of the forces generated by each vehicle's component on each body axis:

$$a_{x_m} = \frac{1}{m}(F_{x_f} + F_{x_w} + F_{x_h} + T_{x_p}) \tag{30}$$

$$a_{y_m} = \frac{1}{m}(F_{y_f} + F_{y_w} + F_{y_h}) \tag{31}$$

$$a_{z_m} = \frac{1}{m}(F_{z_w} + T_{z_h}). \tag{32}$$

V. Extended Kalman Filter for Airspeed Estimation

The states $\boldsymbol{x}$, inputs $\boldsymbol{u}$ and measurement $\boldsymbol{z}$ are defined:

$$\boldsymbol{x} = \begin{bmatrix} u & v & w & \mu_x & \mu_y & \mu_z \end{bmatrix}^T \tag{33}$$

$$\boldsymbol{u} = \begin{bmatrix} a_x & a_y & a_z & p & q & r & \phi & \theta & \psi & \omega_p & \omega_h & \Lambda \end{bmatrix}^T \tag{34}$$

$$\boldsymbol{z} = \begin{bmatrix} V_x^E & V_y^E & V_z^E & a_{x_m} & a_{y_m} & a_{z_m} \end{bmatrix}^T. \tag{35}$$

A classical EKF formulation is used and detailed in Appendix B. All measurements are pre-filtered using a second order Butterworth filter with an empirically chosen cutoff frequency of 5 Hz, to reduce acceleration noise for the model-based component of the filter, at the expense of a slight time-delay. To ensure that lag is not introduced between measurements and inputs, all inputs are filtered with the same cutoff frequency.

A. Process Noise

The derived kinematic equations (Fig. 3) themselves do not present process noise, however, they use inputs that do. For each sensor, its variance is calculated when the vehicle is at rest and used to populate the process noise matrix

$$\boldsymbol{Q} = diag\left(\begin{bmatrix} \sigma_{a_x}^2 & \sigma_{a_y}^2 & \sigma_{a_x}^2 & \sigma_p^2 & \sigma_q^2 & \sigma_r^2 & \sigma_{\mu_x}^2 & \sigma_{\mu_y}^2 & \sigma_{\mu_z}^2 \end{bmatrix}\right). \tag{36}$$

The resulting numerical values are enumerated in Tab. 2. The vertical wind μ_z covariance is set arbitrarily to a value 10 times smaller than the horizontal winds μ_x and μ_y, as vertical wind is assumed to be close to zero and with limited gusts.

The optimal covariance to model the wind dynamics is obtained by minimizing the Root Mean Square Error (RMSE) between the filter's airspeed estimation and the airspeed measured by a pitot tube installed onboard. For the six flights presented in Tab. 5, wind covariance is cycled through values ranging from 1×10^{-8} to 1×10^{-2} leading to Fig. 3.

The RMSE is minimized for a wind covariance within 1×10^{-6} to 2×10^{-4} $\mathrm{m^2\,s^{-2}}$. A high value of 1.25×10^{-4} $\mathrm{m^2\,s^{-2}}$ within the range was chosen to allow the wind estimation to adapt fast enough for gusts, but not to adjust excessively to measurement errors and lead to a wrong wind estimation.

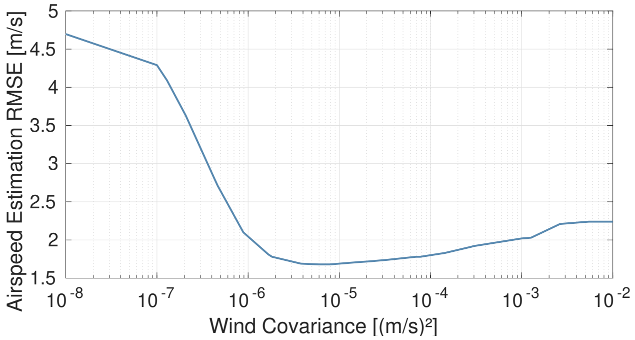

Fig. 3 Wind covariance tuning by minimizing airspeed estimation RMSE.

	Q
$\sigma^2_{a_x}$ $(\mathrm{m/s^2})^2$	1.2×10^{-4}
$\sigma^2_{a_y}$ $(\mathrm{m/s^2})^2$	6.2×10^{-4}
$\sigma^2_{a_z}$ $(\mathrm{m/s^2})^2$	3.0×10^{-4}
σ^2_{p} $(\mathrm{rad/s})^2$	3.1×10^{-9}
σ^2_{q} $(\mathrm{rad/s})^2$	1.2×10^{-9}
σ^2_{r} $(\mathrm{rad/s})^2$	1.3×10^{-9}
$\sigma^2_{\mu_x}$ $(\mathrm{m/s})^2$	1.25×10^{-4}
$\sigma^2_{\mu_y}$ $(\mathrm{m/s})^2$	1.25×10^{-4}
$\sigma^2_{\mu_z}$ $(\mathrm{m/s})^2$	1.25×10^{-5}

	R
$\sigma^2_{V_x}$ $(\mathrm{m/s})^2$	4.1×10^{-5}
$\sigma^2_{V_y}$ $(\mathrm{m/s})^2$	4.2×10^{-5}
$\sigma^2_{V_z}$ $(\mathrm{m/s})^2$	1.4×10^{-4}
$\sigma^2_{a_{xm}}$ $(\mathrm{m/s^2})^2$	5×10^{-5}
$\sigma^2_{a_{ym}}$ $(\mathrm{m/s^2})^2$	1×10^{-4}
$\sigma^2_{a_{zm}}$ $(\mathrm{m/s^2})^2$	5×10^{-4}

Table 2 Covariance assumptions for process and measurement noise of EKF filter. Sensor noise was obtained by measuring variance with the vehicle at rest.

B. Measurement Noise

The measurement noise is defined as:

$$\boldsymbol{R} = diag\left(\begin{bmatrix}\sigma^2_{V_x} & \sigma^2_{V_y} & \sigma^2_{V_z} & \sigma^2_{a_{xm}} & \sigma^2_{a_{ym}} & \sigma^2_{a_{zm}}\end{bmatrix}\right). \tag{37}$$

It is assumed to be zero mean and Gaussian. For GNSS velocities, the measurement noise is the sensor noise. The acceleration measurement noise a_{i_m} contains the addition of sensor noise and modelling noise. It is assumed to be zero mean and Gaussian. It is hand tuned to provide good filter performance.

C. Initial Conditions

The EKF's initialization occurs once the aircraft has taken off. This precautionary measure ensures that the filter is not running while on the ground. As body velocities and wind speed are unknown at initialization, they are set to 0, as are the offsets. The initial covariance matrix is set to the identity matrix, except for the wind states, which are set to their process noise $\boldsymbol{Q}$ value.

D. Covariance Modifications

To accelerate convergence of the wind estimation to its steady state value, the wind process noise is multiplied by 100 for the first 20 s of flight. This was tuned empirically to allow for quick convergence. The z axis acceleration model only provides airspeed information once the wing starts producing lift. Therefore, its covariance is increased when the skew angle is smaller than 60°. A gain K_{a_z} is scheduled between two hand tuned skew angle set points:

$$K_{a_z} = \begin{cases} 10\text{\^{}}2, & \text{if } \Lambda \leq 60^\circ \\ 10\text{\^{}}(\frac{-2\,(\Lambda-70)}{70-60}), & \text{if } 60^\circ < \Lambda < 70^\circ \\ 10\text{\^{}}0, & \text{Otherwise.} \end{cases} \tag{38}$$

The gain is multiplied with the existing acceleration measurement covariance. This scheduling allows a smooth transition into using the z axis during a transition.

VI. Fault Tolerance and Detection

The airspeed estimation is used to detect sensor failures using a simple thresholding method.

A. Pitot Tube Fault Detection

Two types of pitot tube faults are to be detected: incipient and abrupt, modeled as ramp and step response, respectively. The pitot tube's measurement is compared to the EKF's airspeed estimation to obtain the pitot tube's residual r. To identify a fault, a thresholding operation is performed on the residual's low-pass filtered signal using two criteria:

1) $|r| \geq Z_{norm}$ for a time T_{norm}
2) $\left|\frac{dr}{dt}\right| \geq Z_{deriv}$ for a time T_{deriv},

with Z being a threshold and T a threshold time condition.

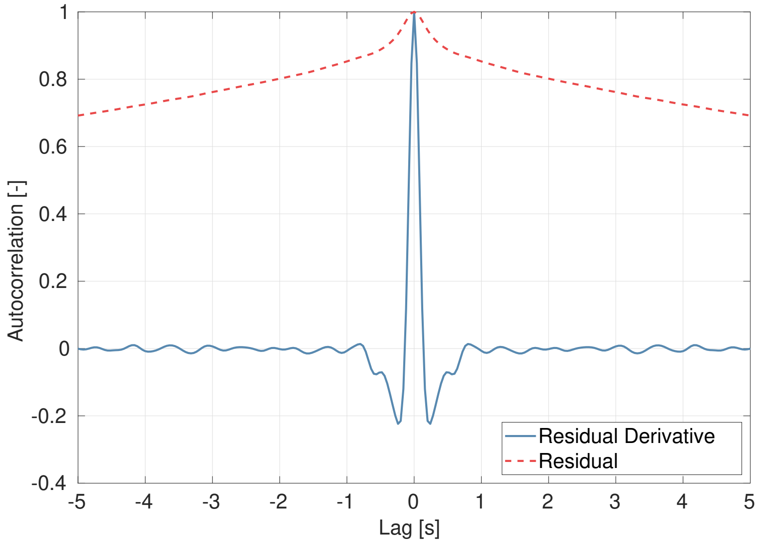

Fig. 4 Autocorrelation for the pitot tube residual and residual's derivative, using airspeed estimation results for 23 test flights (over 2 hours of flight time).

The thresholds and time conditions must be selected as a compromise between rapid failure detection and limiting false detections. A threshold set too low will not allow fault detection while a threshold set too high will lead to false detections. Estimating the likelihood of positive detection is more challenging and will be evaluated experimentally.

A statistical approach is used to select thresholds and timing values to reach a desired false detection rate. Assuming non-correlated signals, the probability p_{seq} of the absolute value of a signal sequence to be be higher than a threshold Z for a set time T is derived:

$$p_{seq} = {p_{single}}^{f_{EKF}\,T}, \tag{39}$$

where f_{EKF} is the frequency of the filter and p_{single} the probability of the signal's absolute value being higher than the threshold for a single occurrence. The false detection's probability per flight hour T_h can be found as:

$$p_h = 1 - \left(1 - p_{seq}\right)^{T_h\, f_{EKF}} . \tag{40}$$

A rate of $< 0.1\%$ false detection rate per flight hour is used to select thresholds. It can be modified depending on the vehicle's required fault detection time and the operator's tolerance to false detections. A false detection would result in disregarding a healthy sensor, using an alternate airspeed estimation and landing as soon as possible as airspeed measurements would no longer be redundant.

The residuals for 23 flights were compiled to compute the pitot tube's residuals distribution and autocorrelation. As shown in Fig. 4, autocorrelation for the derivative is minimal and allows Eq. 40 to be used. The residual's derivative distribution is shown in Fig. 5. The area under the curve is used to compute the residual's probability of exceeding a certain threshold.

The pitot tube's residual autocorrelation is significantly higher than its derivative, hypothesized to be a result of the wind estimation slowly changing and increasing the likelihood of the residual being correlated to last values. A false detection probability cannot be calculated statistically using the above method due to the higher autocorrelation. Thresholds are hand-tuned to ensure that false detection does not occur during flights.

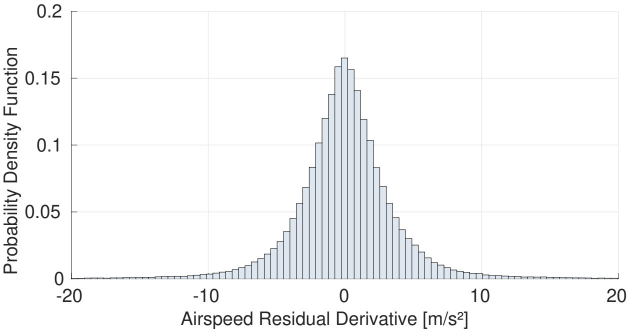

Fig. 5 Distribution of the pitot tube's residual derivative. The histogram is used to estimate false detection rate.

The selected thresholds are presented in Tab. 3. The time thresholds for the residual's derivative are low, as fast changes in residual need to be detected rapidly as they are indications of an abrupt pitot tube failure. To ensure a low false detection rate, derivatives' threshold values are high. The pitot tube residual threshold value is high, as the residuals can occasionally reach such high values during normal operation at the start of flight when the wind estimation has not fully converged. Pitot tube fault detection could be inhibited during that phase of flight, but this would limit the detection capabilities when the pitot tube is first used near the ground.

Component	Threshold Value	Time Threshold [s]	Cutoff Frequency [Hz]	False Detection Probability [% per flight hour]
Pitot Tube Res.	$5.5\ \mathrm{m\,s^{-1}}$	0.25	5	-
Pitot Tube Res. Derivative	$25\ \mathrm{m\,s^{-2}}$	0.12	5	4×10^{-2}
V^E Innov.	$2.5\ \mathrm{m\,s^{-1}}$	0.08	5	7×10^{-2}
V^E Innov. Derivative	$30\ \mathrm{m\,s^{-2}}$	0.08	5	2×10^{-3}
a_{x_m} Innov.	$1.25\ \mathrm{m\,s^{-2}}$	2	0.1	$< 1 \times 10^{-6}$
a_{x_m} Innov. Derivative	$250\ \mathrm{m\,s^{-3}}$	0.12	0.1	5×10^{-5}

Table 3 Thresholds selected for pitot tube detection and sensor fault detection using statistical analysis.

B. EKF Fault Tolerance

If a sensor feeding the estimation system fails without being detected, the precision of the estimation diminishes. The drop in precision might be attributed to a pitot tube failure while the failure may lie within the filter itself. It is crucial to detect sensor faults before the pitot tube fault detector can attribute them to a pitot tube fault.

First, we consider the accelerations, Euler angles and angular rates to be fault free, as they are estimated by a state estimation filter that can be made triple redundant*. The Euler angles are used to convert ground speed measurements from the NED frame to the body frame (see Eq. 2). Without them, no ground speed measurement could be used for the state update. Additionally, the accelerations, Euler angles and angular rates are used directly in the state update equations (refer to Fig. 3). Their absence would render the state prediction and the whole EKF inoperative.

Measurement innovation is defined as the difference between the EKF's expected measurement value and its actual measurement value. Various sensor failures will have effects on different innovation values, as derived in Tab. 4. This table was built by identifying where each sensor is used in the model-dependent and independent equations. A similar strategy as for the pitot tube fault detection is used, with one detector for each EKF's measurement innovation. Once a fault is detected, the filter does not update the state with the measurement and increases its covariance to represent the measurement's faulty state.

Failure Type **Impact Innovation**	**Pitot**	**GNSS**	**Skew Sensor**	**RPM Hover**	**RPM Push**
Pitot	X				
V_x^E		X			
V_y^E		X			
V_z^E		X			
a_{x_m}			X		X
a_{y_m}			X	X	
a_{z_m}			X	X	

Table 4 Innovation impact depending on failure. Table can be interpreted as such: if a failure occurs on a specific sensor (column), it will impact specific innovation values (rows).

Thresholds are selected using a similar strategy used for the pitot tube fault detection and are presented in Tab. 3. For the acceleration, the innovation needs to be aggressively filtered. Noise makes it challenging to distinguish small innovation changes due to sensor fault from the background noise. For this work, only thresholds for the x axis innovation acceleration were implemented, but a similar approach can be used for the other axes.

VII. Results and Discussion

This section details the experiments and results used to determine the airspeed estimation precision of the newly developed EKF and its usability to detect pitot tube and sensor faults.

A. Airspeed Estimation

Six test flights with the VSQP were selected to demonstrate the filter's precision in different flight phases and wind conditions, as enumerated in Tab. 5. Flight 1's flight trajectory is shown in Fig. 6 as an example of a typical transition flight. The different measurements and inputs required for the EKF filter are logged during each flight. The filter is ran offline at 25 Hz from raw logged data. The filter's airspeed estimation is compared to the pitot tube's measured airspeed to obtain the error ΔV and subsequent RMSE over the different flight modes. The comparison is completed when the estimated angle of attack and side-slip are within ±25°, the typical range where pitot tube readings are not sensitive to flow angles [22]. The quantitative results for each flight are summarized in Tab. 6.

---

*Refer to PX4's EKF: https://docs.px4.io/main/en/advanced_config/tuning_the_ecl_ekf.html

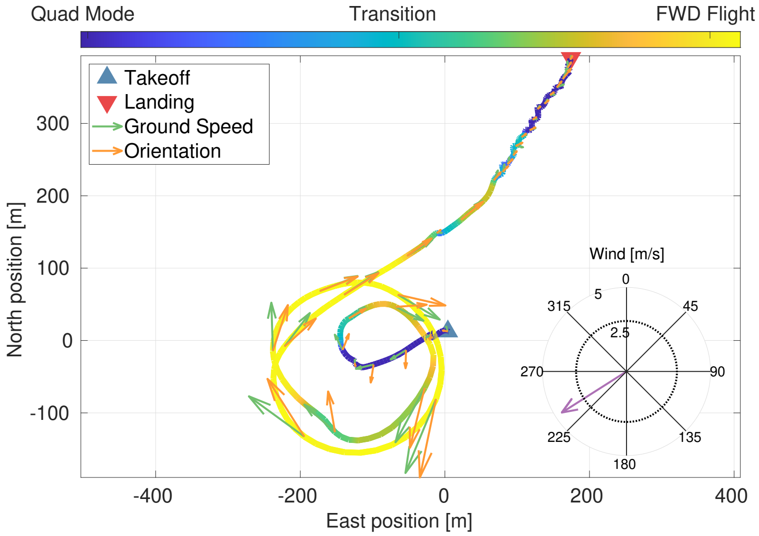

Fig. 6 Flight 1 trajectory, with the skew angle shown as line color. Note the different takeoff and landing points, as the aircraft was launched from a moving ship.

The filter is implemented in C++ in the open source autopilot paparazzi UAV[†] for use in flight. Performance tests on the PX4 Cube Orange main computing board [‡] demonstrated that the filter requires approx. 140 µs per cycle, leaving ample time for other autopilot processes.

1. Overall Results

The average RMSE between airspeed estimation and pitot tube readings for all flights is $1.62\,\mathrm{m\,s^{-1}}$, with an average error of $-0.49\,\mathrm{m\,s^{-1}}$. Using a completely model-independent EKF, Rhudy et al. [5] obtained a better overall average error of $0.22\,\mathrm{m\,s^{-1}}$, albeit by using angle of attack and side-slip vanes on a conventional fixed wing vehicle. For a model-dependent method based on the lift coefficient, Youn et al. [6] obtain a slightly higher $1.89\,\mathrm{m\,s^{-1}}$ RMSE. Considering our method is not using additional angle of attack or side slip sensors, it provides airspeed estimation results comparable to the model-dependent and independent method on which it was based. Contrary to the two methods cited, our strategy is able to estimate airspeed in all flight phases of the vehicle.

The RMSE in quad mode is on average twice as large compared to forward flight. The increased error in quad mode can be attributed to three different factors. First, there is generally less movement to estimate wind and airspeed using the ground speed measurement. The filter has to rely on the acceleration model-dependent airspeed estimation. Additionally, propeller-induced vibrations introduce increased noise levels during hover. This creates challenges for extracting the necessary acceleration signal for accurate airspeed estimation. Finally, the accuracy of pitot tubes generally decreases with airspeed [23]. As it is used as a reference, in low speed hover flight, its reduced precision could increase the hover flight RMSE.

In forward flight, the estimation error is reduced compared to quad mode. Ground speed, x and z acceleration measurements can be used to estimate the airspeed, providing higher precision. Additionally, acceleration noise is reduced, providing easier airspeed estimation from acceleration measurements.

In transition, the higher RMSE compared to forward flight can in part be attributed to the changing wing dynamics in transition and possible imprecision of the wing model when skewed. In flight 4, which was flown with a sustained wing skew, the RMSE is increased, as is the average error ΔV. Again, this points to some model uncertainty that offsets the airspeed estimate. For example, the wing model could be overestimating the lift at a set skew angle, leading to a lower airspeed to be propagated in the filter.

[†] `https://github.com/paparazzi/`

[‡] `https://ardupilot.org/copter/docs/common-thecubeorange-overview.html`

Flight	Flight Type	Average Wind Speed $[\mathrm{m\,s^{-1}}]$	Flight Duration		
			Total [s]	Quad Mode [s]	Forward Flight [s]
1	Transition	4.6	352	169	79
2	Transition	5.7	241	140	92
3	Transition	5.3	310	155	139
4	Wing Skewed 30-60 degrees	9.1	227	164	0
5	Hover Flight	7.6	307	307	0
6	Pitot Tube Failure	7.0	338	249	0

Table 5 Flight selection for testing the EKF filter, with different flight types and wind speeds.

Flight	RMS ΔV $[\mathrm{m\,s^{-1}}]$				average(ΔV) $[\mathrm{m\,s^{-1}}]$
	Full Flight	Quad Mode	Transition	Forward Flight	
1	1.25	1.70	1.14	0.91	-0.14
2	1.42	2.06	1.80	0.75	-0.82
3	2.03	2.58	1.40	1.29	1.12
4	1.91	2.04	1.56	-	-1.34
5	1.50	1.62	-	-	-0.75
6	1.64	1.73	-	-	-0.99
Average	1.62	1.95	1.47	0.98	-0.49

Table 6 Airspeed error for selected flights, comparing between EKF's estimation and pitot tube measurements. Transition is defined as a skew angle between 30–80°. RMSE is smallest in forward flight and biggest in quad mode.

2. Closer Examination of a Single Flight

Flight 3 shows higher error values than other flights due to various factors. It warrants a closer examination in Fig. 7. The vehicle takes off in quad mode ($\Lambda = 0°$). As the vehicle took off, the wind covariance is increased, leading to the wind estimation to quickly converge in about 10 s to its steady state value.

At $t = 350$ s, the vehicle starts its transition to forward flight, with the airspeed estimation closely following the pitot tube measurement. Once in forward flight ($\Lambda = 90°$), the aircraft travels in circles with the airspeed estimation oscillating slightly, at the same period as the wind estimation. This is due to a slight side-slip angle offset varying throughout the circle that is not captured by the filter, generating an oscillating wind estimation to compensate. This increases the forward flight RMSE slightly compared to other flights.

At $t = 545$ s, the drone comes back to its landing pad and descends slowly. An offset between pitot tube and airspeed estimation builds up starting from $t = 550$ s. This is assumed to be due to the reduction in wind velocity close to the ground, as the landing pad is sheltered from the wind. The filter's wind estimation magnitude does decrease slowly, but not rapidly enough, contributing to the increased hover airspeed estimation error.

B. Pitot Tube Fault Detection

1. Abrupt Fault

The ability of the thresholding method to detect abrupt pitot tube faults was validated using real flight test data where a fault was present. An abrupt pitot tube fault occurred during flight 6 at $t \approx 311.9$ s, as shown in Fig. 8a. The fault is first detected by the derivative criterion in 0.16 s and later by the normal criterion. The derivative criterion detected the fault earlier than the normal residual criterion, as the abrupt fault is characterized by a rapidly changing airspeed measurement. Such a quick detection time should allow sufficient time for the autopilot to switch to the synthetic airspeed estimation before loss of stability.

Both the normal and derivative criteria detection time are longer than their time threshold (0.25 and 0.12 s respectively) due to the delay induced by filtering the residual. Increasing the low pass filter's cutoff frequency would reduce the delay, but would require a higher threshold to guarantee the same low false detection rate.

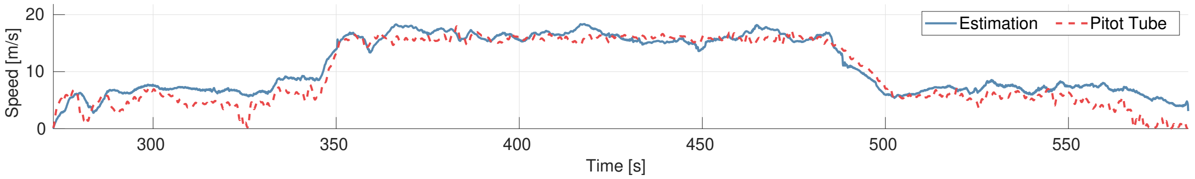

(a) Airspeed estimation

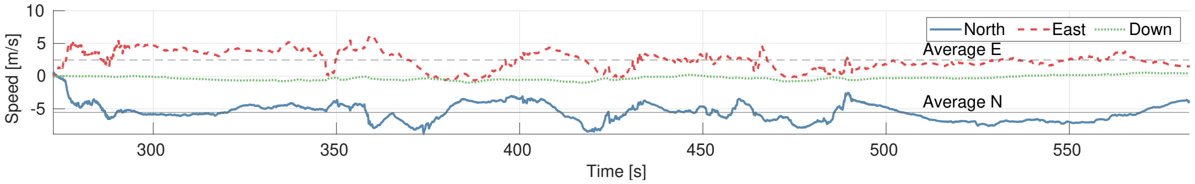

(b) Wind Estimation in NED Frame

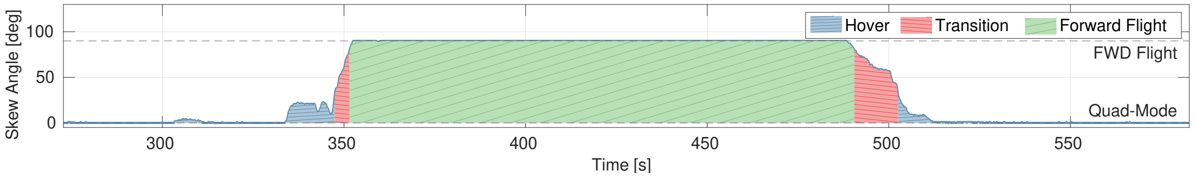

(c) Skew Angle

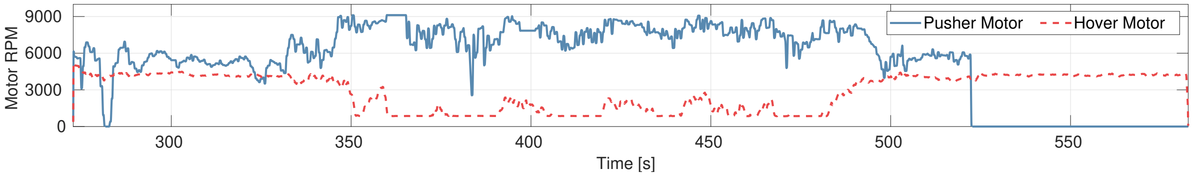

(d) RPM Motor Commands

Fig. 7 Flight 3 with full transition from quad to forward flight mode at $t = 350\,\mathrm{s}$. Overall $2.03\,\mathrm{m\,s^{-1}}$ RMSE, hover RMSE $2.58\,\mathrm{m\,s^{-1}}$, transition $1.40\,\mathrm{m\,s^{-1}}$ RMSE, forward flight $1.29\,\mathrm{m\,s^{-1}}$ RMSE

2. *Incipient Fault*

The incipient fault is simulated on flight 2 as a negative ramp with a $-2.5\,\mathrm{m\,s^{-2}}$ rate, simulating a water blockage [1]. Fig. 8b shows a detection only occurring after 2.5 s, resulting in an approx. $7\,\mathrm{m\,s^{-1}}$ airspeed error. The long detection time is due to the high $6\,\mathrm{m\,s^{-1}}$ residual threshold required before starting to recognize the behavior as a possible fault. This is a limitation of the thresholding method. A lower threshold could be used, but would lead to false detections at the start of the flight, where the wind is converging to its real value. Other methods that examine the statistical mean and variance of the signal such as generalized likelihood tests [24] can be explored to reduce detection time. These come at the expense of additional computing power, as a statistical model needs to be fitted to the residual signal in real time to see if this model changes over time.

C. EKF Fault Tolerance

To validate the EKF's ability to tolerate sensor faults and to detect them in time, simulated sensor faults were inserted in flight 2's logged data.

1. *GNSS Fault*

A GNSS failure is simulated in forward flight, by setting the measurement to 0. Fig. 9 shows detection by the derivative criterion in 0.12 s, at which point the GNSS ground speed measurement is no longer used to update the states. As a result, the wind estimation stops being updated and stays constant. The fault results in a $2\,\mathrm{m\,s^{-1}}$ drop in estimated airspeed which would not trigger the pitot tube fault detector. The airspeed estimation converges back to the pitot tube measurement after the fault. Precision after the fault is reduced from 1.55 to $2.23\,\mathrm{m\,s^{-1}}$, due to the reduced number of measurements used to update the airspeed.

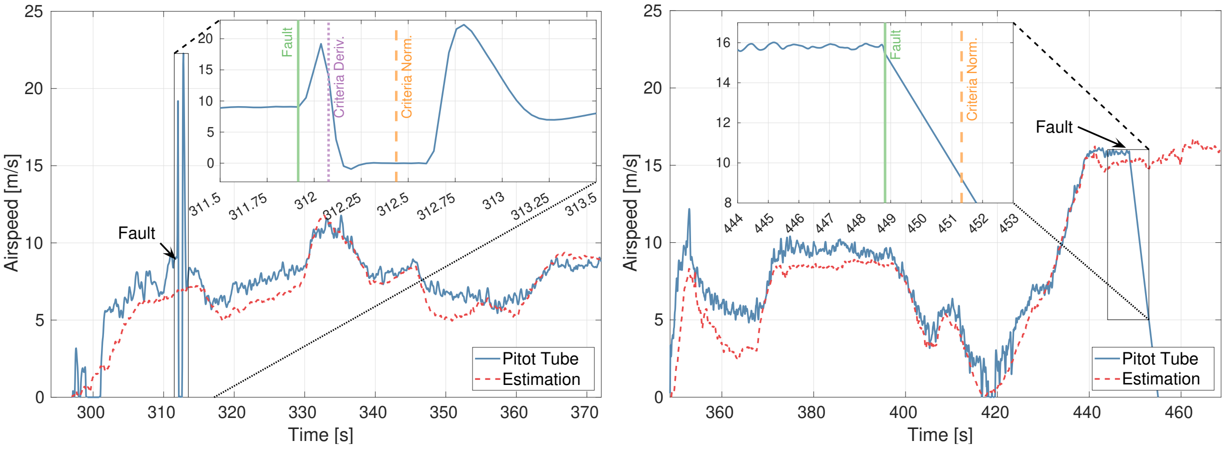

(a) Abrupt pitot failure in flight 6 at $t \approx 311.9\,\mathrm{s}$. Fault is detected in $0.16\,\mathrm{s}$ by the derivative criterion and by the normal criterion $0.36\,\mathrm{s}$ later.

(b) Simulated incipient pitot tube fault at $t = 448.8\,\mathrm{s}$ during flight 2. Detection is achieved in $2.5\,\mathrm{s}$ by the normal residual criterion.

Fig. 8 Pitot tube fault cases.

2. *Pusher RPM Sensor Fault*

A pusher RPM sensor failure is simulated by setting the measured RPM to 0 in forward flight, when it would normally be around 8000 RPM. With RPM at 0 and at a high airspeed, the filter estimates a reduction in airspeed. Fig. 10 shows a $4.3\,\mathrm{s}$ detection time that leads to a $2\,\mathrm{m\,s^{-1}}$ drop in estimated airspeed similar to the GNSS fault.

Airspeed estimation is maintained. As with the GNSS fault, the loss of a measurement leads to a drop in airspeed precision, from 1.55 to $2.33\,\mathrm{m\,s^{-1}}$. It is shown that the filter can tolerate and detect sensor faults. Once a fault is detected, it is recommended to land as the airspeed estimation's precision is reduced and cannot guarantee accurate pitot tube fault detection using the thresholds defined for the fault-free sensor condition.

D. Application to Other Vehicles

To validate that the filter can be applied to hybrid vehicles of a similar configuration with minimal work, the filter was tested on an older VSQP prototype, flying in TU Delft's Open Jet Facility (OJF) wind tunnel [14]. Compared to a normal flight where the vehicle is moving and wind is varying slowly, in the wind tunnel tests, the vehicle is trying to keep its position constant while incoming wind is changed. The wind covariance was increased to model these changes. The sensor covariance was adjusted to fit the sensors installed on the older prototype. The prototype's force model coefficients were identified using flight test data in different configurations. As RPM feedback from the motors was not available, the Pulse Width Modulation (PWM) control signal is used to estimate motor RPM.

Fig. 11 shows three transitions. The overall $1.66\,\mathrm{m\,s^{-1}}$ RMSE is comparable to results with the newest VSQP. Airspeed estimation oscillations can be observed during transition, which seems to be derived from the pusher motor oscillating. In forward flight, the RMSE is low, due to the constant magnitude and gust-free airflow of the wind tunnel.

Overall, the precise airspeed estimation obtained on an older prototype show that the filter can be used on other platforms having a similar configuration. Instead of using wind tunnel data to obtain the coefficients necessary to model the forces, flight test data can be used to empirically estimate them.

VIII. Conclusion

The intent of this work was to develop a synthetic air data system for the Variable Skew Quad Plane (VSQP) hybrid vehicle in order to detect pitot tube failures. An Extended Kalman Filter (EKF) based on kinematic equations using GNSS and inertial measurements was developed. It is augmented using a simplified model of the vehicle and acceleration measurements. Validation on six different test flights lead to an average airspeed Root Mean Square Error (RMSE) of $1.62\,\mathrm{m\,s^{-1}}$ and an average airspeed error of $-0.49\,\mathrm{m\,s^{-1}}$. Precision is maximal in forward flight, when all measurements can be used to estimate airspeed and the rotor induced acceleration noise is minimal. The airspeed estimation was able to detect a real-life abrupt pitot tube fault in $0.16\,\mathrm{s}$ using a simple residual thresholding method. A similar approach was shown to provide fault tolerance to the filter, ensuring that sensor faults do not lead to a wrong

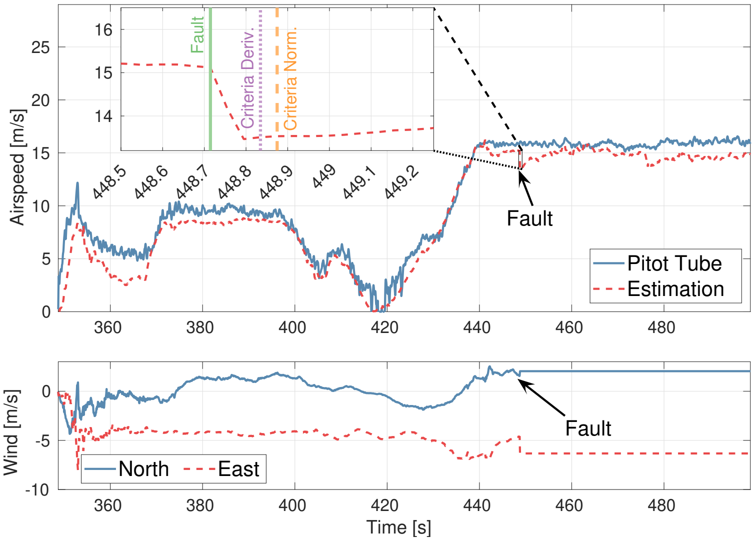

Fig. 9 Simulated GNSS Failure at $t = 448$ s during flight 2. Detection is achieved in 0.12 s, leading in a $2\,\mathrm{m\,s^{-1}}$ airspeed estimation drop.

airspeed estimation and to false pitot tube failure detection. One of the biggest benefits of the developed EKF filter is its ability to estimate airspeed for the whole flight envelope of the hybrid vehicle using conventional GNSS and inertial sensors, without the use of angle of attack or side slip vanes.

A. Recommendations

Additional work should examine how to improve the force models to reduce the average airspeed estimation error. To guide this research, the authors recommend to analyze the effect of each model component (fuselage, wing, pusher propeller, hover propeller) on the precision of the airspeed estimation. Such a sensitivity analysis would contribute to a better understanding of the robustness of model-dependent airspeed estimation in relation to variations in vehicle characteristics.

The airspeed estimation filter was initially developed as to be completely independent from the pitot tube. Integration of the pitot tube as a measurement into the filter should be considered, for which faults are monitored on each measurement's innovation. Such a system would improve the airspeed estimation during fault-free flight and group the airspeed estimation and fault detection functions in a single, easier to implement package on the vehicle.

Alternative detection methods based on statistical signal analysis should also be explored. They could provide a shorter detection time that be less affected by the measurement noise. These could identify the change in mean or standard deviation that occurs on innovation after a fault, while being more robust to noise. This would directly improve the detection time for the incipient fault. Although they might require increased computing power, they could potentially offer better and more robust fault protection.

Finally, if the filter's airspeed estimation is to be ultimately used for control of the vehicle, further research should go into characterizing and understanding the interaction between the estimation and control aspects. For example, pusher RPM oscillations have been seen to lead to airspeed estimation oscillations. These should be contained as to not lead to control oscillations, that could be amplified by the estimation process, leading to instability.

Acknowledgments

Funded with support of the Royal Dutch Navy and the Royal Coast Guard, this initiative aims to foster collaboration and innovation in maritime endeavors.

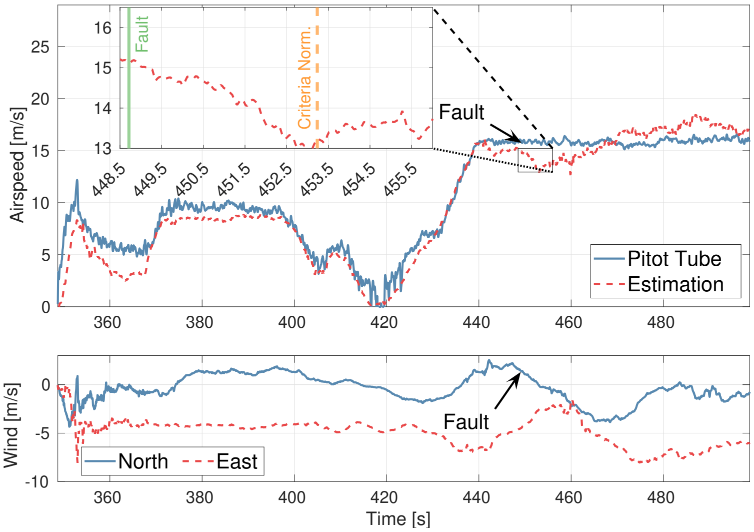

Fig. 10 Simulated pusher RPM sensor failure at $t = 448\,\mathrm{s}$ during flight 2. Detection is achieved in 4.3 s and leads to a $2\,\mathrm{m\,s^{-1}}$ airspeed estimation drop.

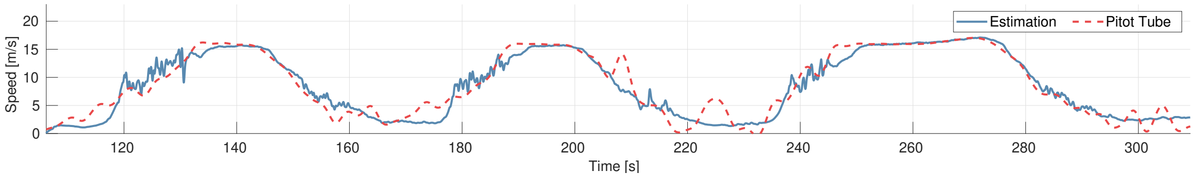

(a) Airspeed estimation

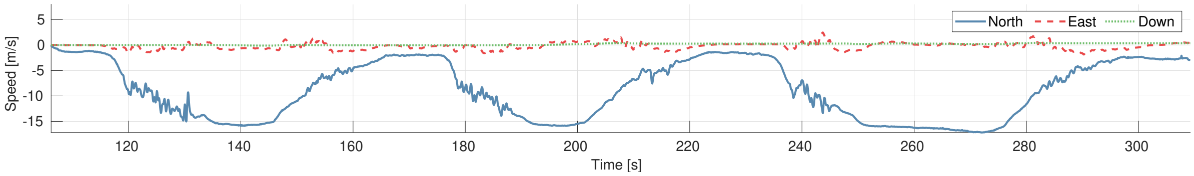

(b) Wind Estimation in NED Frame

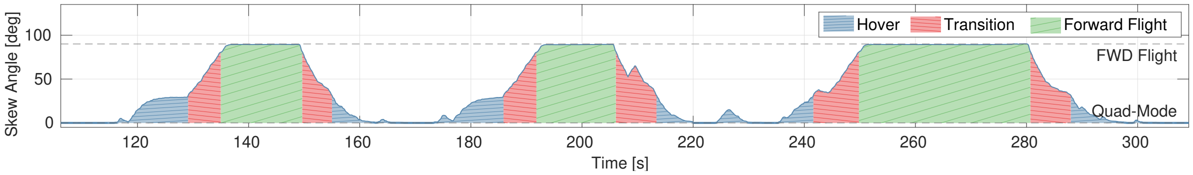

(c) Skew Angle

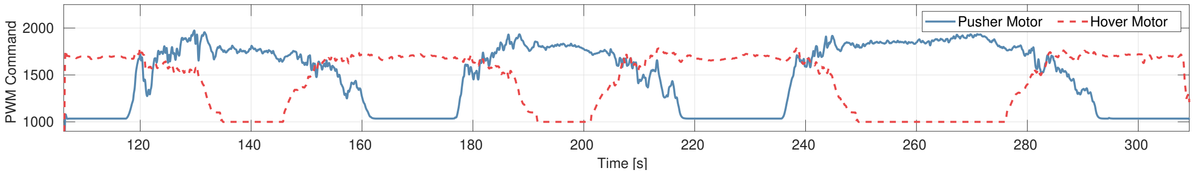

(d) PWM Motor Commands

Fig. 11 Airspeed estimation during wind tunnel flights with the older VSQP prototype. Wind is increased and decreased while the model tries to hold its position. Overall $1.66\,\mathrm{m\,s^{-1}}$ RMSE, hover $1.92\,\mathrm{m\,s^{-1}}$ RMSE, Transition $2.06\,\mathrm{m\,s^{-1}}$ RMSE, forward flight $0.40\,\mathrm{m\,s^{-1}}$ RMSE. Note that North is defined as pointing towards the wind tunnel and airflow.

References

[1] Sun, K., and Gebre-Egziabher, D., "Air data fault detection and isolation for small UAS using integrity monitoring framework," *Institute of Navigation*, Vol. 68, No. 3, 2021, pp. 577–600. https://doi.org/10.1002/navi.440.

[2] R.P.G Collinson, *Introduction to Avionics Systems*, 3rd ed., Springer, New York, 2011.

[3] Downer, J., *When failure is an option : redundancy, reliability and regulation in complex technical systems*, Centre for Analysis of Risk and Regulation at the London School of Economics and Political Science, London, 2009.

[4] Alvarez, O. H., "Fault Tolerant Air Data System for Pitot Tube Failure," Ph.D. thesis, Universidad Pontificia Bolivariana, Medelin, 2020. URL http://hdl.handle.net/20.500.11912/7362.

[5] Rhudy, M. B., Fravolini, M. L., Gu, Y., Napolitano, M. R., Gururajan, S., and Chao, H., "Aircraft model-independent airspeed estimation without pitot tube measurements," *IEEE Transactions on Aerospace and Electronic Systems*, Vol. 51, No. 3, 2015, pp. 1980–1995. https://doi.org/10.1109/TAES.2015.130631.

[6] Youn, W., Ryu, H., Jang, D., Lee, C., Park, Y., Lee, D., and Rhudy, M. B., "Model-Aided Synthetic Airspeed Estimation of UAVs for Analytical Redundancy," *IEEE Robotics and Automation Letters*, Vol. 6, No. 3, 2021, pp. 5841–5848. https://doi.org/10.1109/LRA.2021.3086428.

[7] Hansen, S., and Blanke, M., "Diagnosis of Airspeed Measurement Faults for Unmanned Aerial Vehicles," *IEEE Transactions on Aerospace and Electronic Systems*, Vol. 50, No. 1, 2014. https://doi.org/10.1109/TAES.2013.120420.

[8] Neumann, P. P., and Bartholmai, M., "Real-time wind estimation on a micro unmanned aerial vehicle using its inertial measurement unit," *Sensors and Actuators, A: Physical*, Vol. 235, 2015, pp. 300–310. https://doi.org/10.1016/J.SNA.2015.09.036.

[9] Hattenberger, G., Bronz, M., and Condomines, J. P., "Estimating wind using a quadrotor," *International Journal of Micro Air Vehicles*, Vol. 14, 2022. https://doi.org/10.1177/17568293211070824.

[10] Leishman, R. C., Macdonald, J. C., Beard, R. W., and McLain, T. W., "Quadrotors and Accelerometers: State Estimation with an Improved Dynamic Model," *IEEE Control Systems Magazine*, Vol. 34, No. 1, 2014, pp. 28–41. https://doi.org/10.1109/MCS.2013.2287362.

[11] Van Wijngaarden, D. C., Smeur, E. J. J., and Remes, B. W. D., "Flight Code Convergence: Fixedwing, Rotorcraft, Hybrid," *12th International Micro Air Vehicle Conference*, 2021, pp. 21–27.

[12] Hirschberg, M. J., Hart, D. M., and Beutner, T. J., "A summary of a half-century of oblique wing research," *Collection of Technical Papers - 45th AIAA Aerospace Sciences Meeting*, Vol. 3, 2007, pp. 1781–1815. https://doi.org/10.2514/6.2007-150.

[13] Van Wijngaarden, D. C., and Remes, B. D. W., "INDI Control for the Oblique Wing-Quad Plane Drone," *International Micro Air Vehicle Conference*, Delft, 2022, pp. 119–126.

[14] De Ponti, T. M. L., Smeur, E., and Remes, B., "Incremental Nonlinear Dynamic Inversion Controller for a Variable Skew Quad Plane," *2023 International Conference on Unmanned Aircraft Systems (ICUAS)*, Warsaw, 2023, pp. 241–248.

[15] Smeur, E., Chu, Q., de Croon, G., Remes, B., Wagter, C. D., and van der Horst, E., "Modelling of a Hybrid UAV Using Test Flight Data," *International Micro Air Vehicle Competition and Conference 2014*, Delft, The Netherlands, 2014, pp. 196–203. https://doi.org/10.4233/uuid:ef248460-783a-4894-bc3b-668304715a60.

[16] Smeur, E. J. J., Bronz, M., and de Croon, G. C. H. E., "Incremental Control and Guidance of Hybrid Aircraft Applied to a Tailsitter UAV," *Journal of Guidance, Control, and Dynamics*, Vol. 43, No. 2, 2018. https://doi.org/10.2514/1.G004520, URL http://arxiv.org/abs/1802.00714.

[17] Rhudy, M. B., Fravolini, M. L., Porcacchia, M., and Napolitano, M. R., "Comparison of wind speed models within a Pitot-free airspeed estimation algorithm using light aviation data," *Aerospace Science and Technology*, Vol. 86, 2019, pp. 21–29. https://doi.org/10.1016/j.ast.2018.12.028.

[18] Smeur, E. J., Chu, Q., and De Croon, G. C., "Adaptive incremental nonlinear dynamic inversion for attitude control of micro air vehicles," *Journal of Guidance, Control, and Dynamics*, Vol. 39, No. 3, 2016, pp. 450–461. https://doi.org/10.2514/1.G001490.

[19] Burton Brandt, J., *Small Scale Propeller Performance at Low Speed*, Master's Thesis, 2005.

[20] Theys, B., Dimitriadis, G., Andrianne, T., Hendrick, P., and De Schutter, J., "Wind Tunnel Testing of a VTOL MAV Propeller in Tilted Operating Mode," *International Conference on Unmanned Aircraft Systems*, Orlando, 2014, pp. 1064–1072. https://doi.org/10.1109/ICUAS.2014.6842358.

[21] Morikawa, Y., and Tsuchiya, T., "H-Force of Rigid Rotor in Forward Flight of Multi-rotor," *International Symposium on Aerospace Technology*, Vol. 912, 2023, pp. 595–606. https://doi.org/10.1007/978-981-19-2689-1{_}46.

[22] Benedict, R. P., *Fundamentals of Temperature, Pressure, and Flow Measurements*, third edition ed., Wiley-Interscience, 1984.

[23] Buscarini, I. D. O., Barsaglini, A. C., Jabardo, P. J. S., Taira, N. M., and Nader, G., "Impact of Pitot tube calibration on the uncertainty of water flow rate measurement," *Journal of Physics: Conference Series*, Vol. 648, Institute of Physics Publishing, 2015, pp. 1–10. https://doi.org/10.1088/1742-6596/648/1/012005.

[24] Hansen, S., Blanke, M., and Adrian, J., "Diagnosis of UAV Pitot Tube Defects Using Statistical Change Detection," *IFAC Proceedings Volumes*, Vol. 43, No. 16, 2010, pp. 485–490. https://doi.org/10.3182/20100906-3-IT-2019.00084.

[25] James Morris, S., "Integrated Aerodynamic and Control System Design of Oblique Wing Aircraft," Ph.D. thesis, Stanford, 1 1990. URL https://ntrs.nasa.gov/search.jsp?R=19930074026.

Appendix A. Model Validation

The force models presented in Sec. IV were validated using wind tunnel data obtained at TU Delft's OJF. The model is set on a pole connected to a 6-component balance measuring forces and moments. The assembly is placed on a turntable to submit the vehicle to different angles of attack or side-slip angles, as shown in Fig. 12.

Fig. 12 Static test in TU Delft's OJF wind tunnel. The VSQP is placed on a 6-component balance that is rotated through 360° to subject the vehicle to various angle of attack and side-slip conditions.

Different test rounds are completed with the same wind speed, angle of attack, side-slip and actuator commands, but removing components on the vehicle (wing, elevator, hover propellers, pusher propellers). Specific components of the vehicle can be isolated by subtracting test rounds results with the same parameters.

The coefficients for the force models can be determined by minimizing the average RMSE between model estimation and wind tunnel data points. Fig. 13 to 16 report the wind tunnel data points and the estimation obtained for the fuselage, hover propeller, wing and pusher propeller.

Fig. 14a shows that a constant drag coefficient with angle of attack can be assumed without sacrificing significant fidelity. A second order fit on the angle of attack leads to a slightly better average 0.3 N RMSE compared to the initial 0.6 N RMSE, but results in a more complex model. Fuselage side force is well modeled as linear to side-slip angle in Fig. 14b, with a small 1.21 N average RMSE in comparison to the ±50 N range. Assuming a negligible fuselage z axis force, this leads to a low 1.93 N RMSE, relative to the wing or hover motors that produce approx. 60–70 N.

Fig. 15a and 15c show the relationship between angle of attack and wing F_x and F_z forces. To simplify results, force is divided by the airspeed squared. For a skew angle of 0°, the wing generates minimal body x or z axis force. As skew angle is increased, as modeled by Eq. 27 and 28, the wing generates more force. The F_x wing model developed in Eq. 24 is validated by a $3 \times 10^{-3}\,\mathrm{N/(m/s)^2}$ RMSE. The F_x force becomes positive when approaching an angle of attack of 2–3°, as the lift force is projected forward in the body x-axis and supplants the drag force projection. The F_z wing model developed in Eq. 28 is validated in Fig. 15c with a low $1.7 \times 10^{-2}\,\mathrm{N/(m/s)^2}$ RMSE. Validation for both models was limited to an angle of attack ranging from −5 to 15°, which corresponds to the general flight envelope of the vehicle in forward flight.

Fig. 15b shows an empiric fit linking the side force to the skew angle using trigonometric functions from Eq. 29 with a 0.66 N RMSE for a 6° angle of attack. Side force is underestimated at high skew angles. A fit based on James Morris [25]'s work on oblique wing modelling was also attempted:

$$F_{y_w} = \pm \frac{\cos \Lambda}{\sin \Lambda} \left(\frac{C_L^2}{\pi\, AR\, e} + C_L\, \alpha \right), \tag{41}$$

where the ± is used to specify the side force sign depending on the skew direction (left or right wing forward).

However, the model in Eq. 41 did not properly capture the peak in side force around 30–35° of skew angle. This might be due to some spanwise flow on the wing modifying the lift behavior at low skew angles. Ultimately, Eq. 29 was chosen as it better captured the peak side force.

Hover motor drag force as a function of cross-flow is shown in Fig. 16a, for a normal 3800–4100 RPM hover regime. As expected, the plot highlights a linear relation between hover motor drag force and airspeed, with a slope that increases with RPM. An average value of $-0.75\,\mathrm{N\,s\,m^{-1}}$ from the 4000 RPM curve will be used for further work. For the hover motor thrust force F_z, a quadratic fit with RPM is validated in Fig. 16b with an average 2.5 N RMSE. As predicted, cross-flow has no significant effect.

The pusher propeller thrust force as a function of RPM and airspeed is validated in Fig. 13, with a low 0.42 N RMSE relative to the pusher thrust 30 N range. Thrust force is reduced as airspeed is increased as expected by Eq. 13.

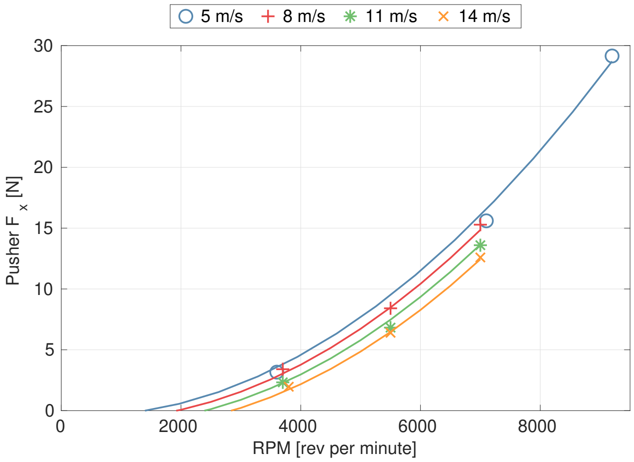

Fig. 13 Pusher motor x-axis force fit depending on RPM for different airspeed. Fit shown is $T_{x_p} = K_{x_{p_1}}\, \omega_p^2 + K_{x_{p_2}}\, \omega_p\, u + K_{z_{p_3}}\, u$, with 0.419 N RMSE.

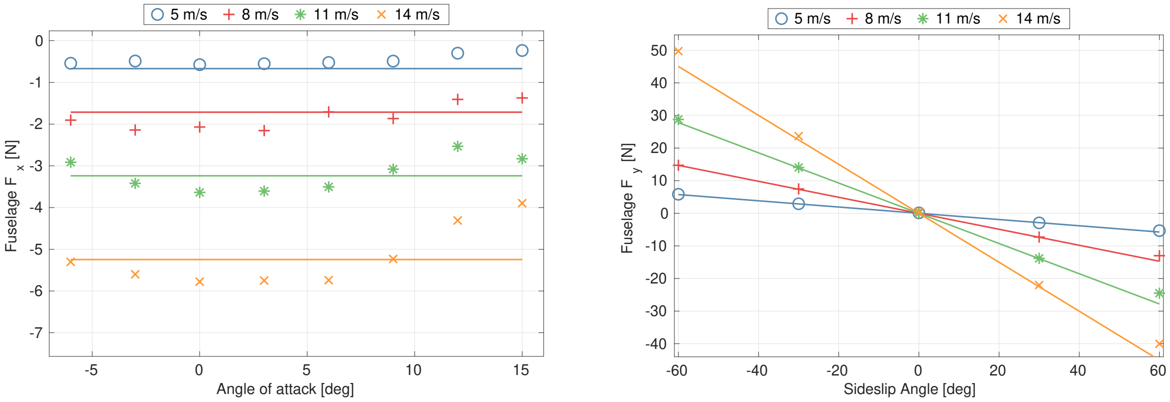

(a) Linear Fit between fuselage x-axis force and angle of attack for different airspeed. Shown fit is $F_{x_f} = K_{x_f}\, u^2$, with 0.6 N RMSE.

(b) Linear Fit between fuselage y-axis force and side-slip angle for different airspeed. Fit shown is $F_{y_f} = K_{y_{f\beta}}\, \beta\, V_a^2$, with 1.21 N RMSE.

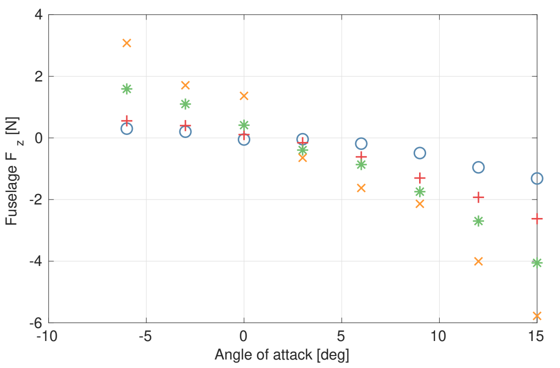

(c) Fuselage z-axis force depending on angle of attack for different airspeed. Fuselage z-axis force was assumed to be negligible, with 1.93 N RMSE.

Fig. 14 Fuselage fit from wind tunnel testing in OJF

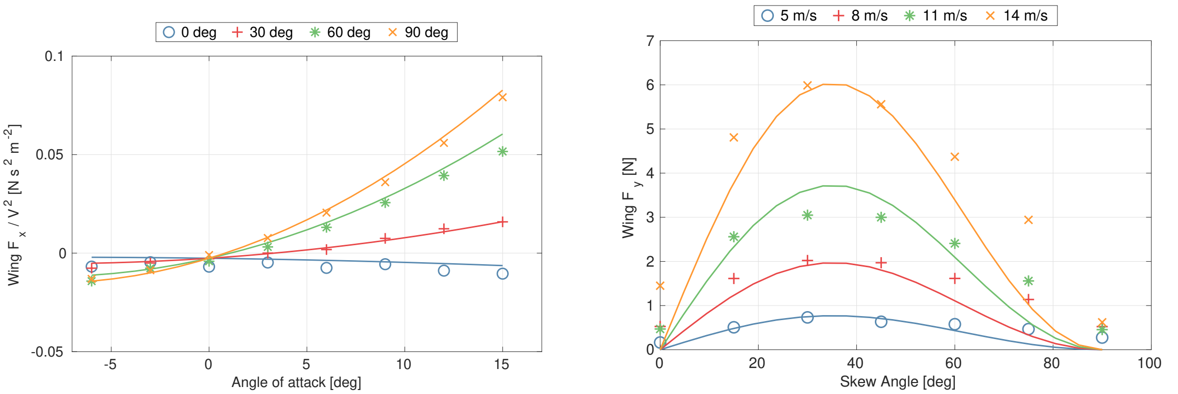

(a) Airspeed scaled wing x-axis force depending on angle of attack for different skew angles. Fit shown is $F_{xw}/u^2 = (K_{xw_0} + K_{xw_1}\ \alpha + K_{xw_2}\ \alpha^2)$, with 0.003 N/(m/s)^2 RMSE.

(b) Wing side force (y-axis) depending on skew angle for a fixed angle of attack of 6°. Fit shown is $F_{yw} = \left(K_{yw}\ \sin\Lambda\cos\Lambda^2\right)\ u^2$, with 0.66 N RMSE.

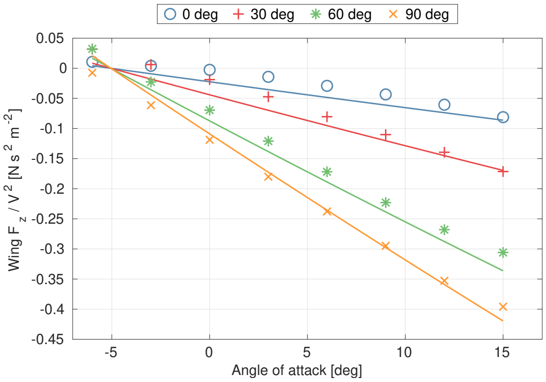

(c) Airspeed scaled wing z-axis force depending on angle of attack for different skew angles. Fit shown is $F_{zw}/u^2 = (K_{zw_0} + K_{zw_1}\ \alpha + K_{zw_2}\ \alpha^2)$, with 0.017 N/(m/s)^2 RMSE.

Fig. 15 Wing fit from wind tunnel testing.

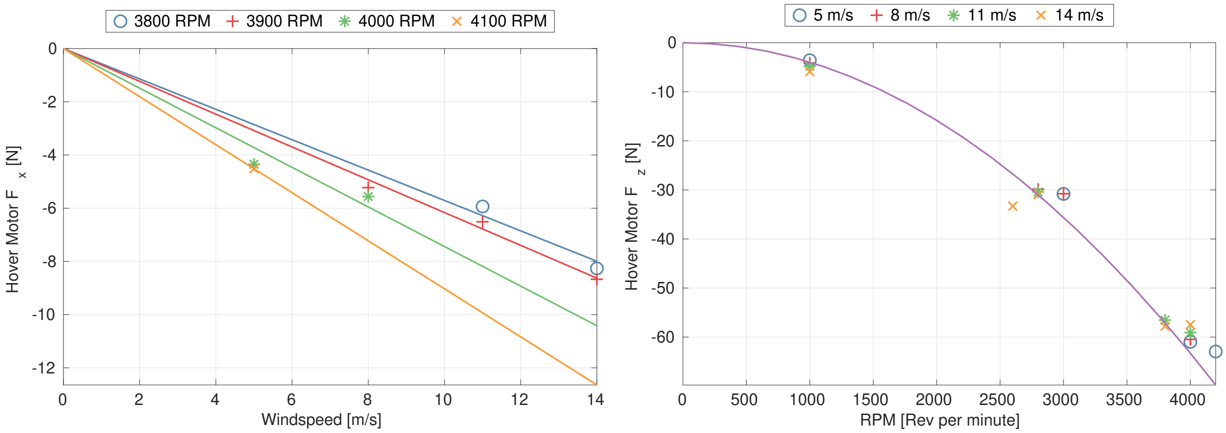

(a) Linear Fit between total hover motor x-axis force and different hover RPM values. Shown fit is $F_{x_h} = K_{x_h}\ u$, with 1.52 N RMSE.

(b) Quadratic Fit between hover motor z-axis force and RPM for different airspeed. Shown fit is $T_{z_h} = K_{z_h}\ \omega_h^2$, with 2.53 N RMSE.

Fig. 16 Hover motor fit from wind tunnel testing.

Appendix B. Extended Kalman Filter Implementation

State vector $\boldsymbol{x}$, input vector $\boldsymbol{u}$ and measurement vector $\boldsymbol{z}$ are defined as:

$$\boldsymbol{x} = \begin{bmatrix} u & v & w & \mu_x & \mu_y & \mu_z \end{bmatrix}^T \tag{42}$$

$$\boldsymbol{u} = \begin{bmatrix} a_x & a_y & a_z & p & q & r & \phi & \theta & \psi & \omega_p & \omega_h & \Lambda \end{bmatrix}^T \tag{43}$$

$$\boldsymbol{z} = \begin{bmatrix} V_x^E & V_y^E & V_z^E & a_{x_m} & a_{y_m} & a_{z_m} \end{bmatrix}^T. \tag{44}$$

With state dynamics $f(x, u)$ and measurement output function $g(x, u)$:

$$\dot{x} = f(x, u) \tag{45}$$

$$z = g(x, u). \tag{46}$$

States, output, state noise and measurement noise Jacobian are respectively $F(x, u)$, $G(x, u)$, $L(x, u)$, $M(x, u)$:

$$F(x, u) = \frac{\partial f}{\partial \boldsymbol{x}} \tag{47}$$

$$L(x, u) = \frac{\partial f}{\partial \mathbf{w}} \tag{48}$$

$$G(x, u) = \frac{\partial g}{\partial \boldsymbol{x}} \tag{49}$$

$$M(x, u) = \frac{\partial g}{\partial \mathbf{w}}. \tag{50}$$

The main equations of the EKF are as follows. First, state and covariance are predicted:

$$\boldsymbol{x}_{pred} = f(x, u)\, dt \tag{51}$$

$$P_{pred} = F(x, u)\, P\, F(x, u)^T + L(x, u)\, Q\, L(x, u)^T. \tag{52}$$

After which innovation and the innovation matrix S are calculated:

$$\boldsymbol{y} = \boldsymbol{z} - g(x, u) \tag{53}$$

$$S = G(x, u)\, P_{pred}\, G(x, u)^T + M(x, u)\, R\, M(x, u)^T. \tag{54}$$

The Kalman Gain can be calculated and used to update the state $\boldsymbol{x}$ and covariance P:

$$K = P_{pred}\, G(x, u)^T\, S^{-1} \tag{55}$$

$$\boldsymbol{x} = \boldsymbol{x}_{pred} + K\, \boldsymbol{y} \tag{56}$$

$$P = (I - K\, G(x, u))\, P_{pred}. \tag{57}$$